scientific reports

Check for updates

OPEN

# Oxygen enriched PAni-based counter electrode network toward efficient dye-sensitized solar cells (DSSCs)

M. Abdelhamid Shahat[1]✉, Ahmed Ghitas[1], Fahad N. Almutairi[2] & Nadi Mlihan Alresheedi[3]

**Dye-sensitized solar cells (DSSCs) have great potential as a renewable energy technology assisting combat climate change due to its low cost, adaptability, and sustainability. Oxygen plasma ion doping is a promising strategy to improve the capacity of a low-cost, platinum-free counter-electrodes (CEs) to absorb photons and drive high-performance DSSCs via generating an abundance of active absorption sites. In this instance, novel PAni–ZnO (PZ) composite layers were designed as a CE material and received various in-situ oxygen plasma dosages, including 0, 2, 4, 6, 8, and 10 min, to improve their physiochemical and microstructural feature for the first time, to the best of our knowledge. Physical evaluations of the microstructure, porosity, morphology, contact angle, roughness, electrical, and optical, electrochemical impedance spectroscopy (EIS) features of CEs were conducted in along with an evaluation of J–V variables. Compared to pristine CE substance, the surface nature of the modified hybrids was gradually enhanced as the plasma level rose, reaching an optimum after 8 min (i.e. 0.2 µm for average pore size and average roughness Ra = 7.21 µm). Expanded plasma treatment doses also improved PV cell performance even further: after 4 min at a plasma level, η = 5.41% was obtained, and after 6 min in a oxygen plasma environment, η = 5.81% was obtained. Mixing high energetic plasma ions increased the mobility of charge carriers in PAni composites along with lowered charge carrier recombination through generating an environment that was conducive to charge dissociation. Therefore, longer lifespans and more effective charge transfer inside the photovoltaic cell as a consequence of the increased mobility less resistive losses. In this respect, following 8 min of plasma surface modification of the PZ CE, the optimized efficiency of 6.31% and $J_{sc}$ of 15.6 mA/cm$^2$ were obtained. The improvement in efficiency equated to a proportion growth of 77% versus a pristine one. This gain was explained by the reality that suffusing a quantity of oxygen plasma free radicals into the PAni system developed continuous channels that enabled the mixture to move electrons more rapidly, hence raising the photovoltaic efficiency. Overall, this study highlights the advantages of regulating heteroatom species and their co-doping, offering a new perspective for the application of heteroatom-doped CE in DSSCs.**

**Keywords** Dye-sensitized solar cells, PAni@ZnO nanocomposites, Counter electrode, In-situ oxygen plasma modifications, Photovoltaics, J–V characteristic curves

Dye-sensitized solar cells (DSSCs) represent a potential renewable energy technology that is suited to dealing with climate change challenges by delivering economical, flexible, and environmentally acceptable solar energy possibilities[1,2]. Considering DSSCs are flexible and semi-transparent, devices may be integrated into architectural features like windows and facades[3]. This versatility broadens the possible uses of solar energy, allowing its integration into a variety of environment and buildings[4]. In addition, DSSCs may easily be integrated with energy storage devices such as batteries or supercapacitors to provide a more constant and reliable energy source[5]. This feature tackles the short-term nature of solar power generation and allows for greater grid integration[6]. Notwithstanding these advantages, there are still obstacles that need to be addressed for widespread adoption of DSSCs, including

[1]PV Unit, Solar and Space Research Department, National Research Institute of Astronomy and Geophysics (NRIAG), Helwan 11421, Cairo, Egypt. [2]Department of Physics, College of Sciences and Humanities, Shaqra University, 19257 Al Quwayiyah, Saudi Arabia. [3]Department of General Studies, Royal Commission for Jubail and Yanbu, Yanbu Industrial College, Yanbu 30436, Kingdom of Saudi Arabia. ✉email: m.abdelhamid999@gmail.com

improving their long-term stability, further enhancing their efficiency, and scaling up production processes. To fulfil all of these demands, several recent research have focused on generating novel compounds with qualitative qualities to improve the efficiency of DSSCs. In general, the photosensitive dye absorbs light, which initiates the working process of DSSCs[7]. Usually, this dye is an organic or metal complex that can absorb a broad spectrum of visible light. Electrons in the dye molecule are excited to a higher energy state when light is absorbed, resulting in the creation of electron–hole pairs[8,9]. While the holes are transported to the dye molecule, the excited electrons from the dye are injected into the metal oxide's conduction band. An electric current is produced as the injected electrons travel through the network of metal oxides in the direction of the conductive substrate. By soaking in the electrons that were released from the dye and moving them to the CE, the electrolyte solution helps the dye molecule regenerate in in the meantime[10]. At the CE (i.e. conductive material), the electrons react with the electrolyte and the holes from the dye to complete the circuit. The surface-active characteristics, affordability, and green credentials of organic compounds—particularly polyaniline, PAni—make it a suitable candidate to generate composite CEs[11]. Moreover, the aforementioned substances can be impregnated with semiconductor component fillers like zinc oxide (ZnO), that perform in conjunction to yield PAni–ZnO (PZ) nanocomposites, providing several of capabilities[12,13]. Given their large surface area and hardness, ZnO nanoparticles (NPs) placed in a PAni matrix improve its electrical, optical, mechanical, and stability characteristics[11]. Likewise, this filler possesses the ability to react with different analytes in the PAni structure, thereby rendering it appropriate for use in conductive coatings, flexible electronics, sensors (such as gas, humidity, and biosensors), and air quality pollution[14,15]. To improve the performance of CE composites for charge carrier excitation, separation, and movements for DSSC usage, researchers are now conducting a number of investigations and experiments focused on PAni-based composites. Researchers are now focused on PAni-based composites for DSSC uses, performing a variety of experiments and evaluations to increase CE performance via simplified charge carrier excitation, separation, and mobility. Ankita Singh et al.[16] improved cell efficiency (i.e., 5.29% for the hybrid system) by fabricating a CE in DSSCs via in-situ polymerization of aniline on $MoSe_2$/rGO nanocomposites. Whereas, loading $NiCo_2O_4$/rGO inside the PAni matrix as a CE raised conversion efficiency of 4.67% for the fabricated DSSCs by Manikandan and et al.[17].

In line with the same objective and to address some gaps, radiofrequency (RF) plasma surface treatment is an appealing method for adjusting the surface qualities of PAni substances.[18–20]. For a variety of applications, including solar cells, this approach could potentially use to boost both the porosity and surface area of PZ composites. In more technical terms, the low-pressure plasma produced by RF generators is capable of producing very energetic ions and radicals that may erode the surface of composite components[18]. This ends up resulting in a rougher surface, microstructures, and surface defects which expand the effective surface area[19]. More reflected photons may be accommodated by a rougher surface, raising the capture effectiveness. Moreover, plasma exposure to the surfaces of such hybrids enhances the volume and interconnectivity of the pores by stimulating their formation and growth. Plasma exposure significantly increases the uniformity of nanofillers in the PAni matrix. A homogeneous dispersion optimizes the surface area available for photon interaction by avoiding nanoparticle aggregation and clustering. In addition, the introduction of functional groups onto the surface of hybrids by plasma exposure may modify both chemical and electrical features. Chemical interactions could identify active locations in these functional groupings[11].

Even with the preceding indicated benefits of the plasma approach on composite surfaces, only limited knowledge about its influence on the structural stability and capability of solar cells is included in the available literature. In this instance, for the first time, a series of innovative PZ layers were designed as a CE and received various in-situ oxygen plasma dosages, including 0, 2, 4, 6, 8, and 10 min, to improve their physiochemical and microstructural feature. Whereas, the surface characteristics of these electrodes, including surface energy, roughness, porosity, hydrophilicity, and reactivity, were enhanced by in-situ oxygen plasma processing. On the other hand, the compound's surface functional groups react with the reactive species in the plasma, introducing novel chemical moieties or effective functional groups (such as OH bonds, vacancies, or C–H zones). These groupings operate as areas of activity for chemical reactions that aid in the carrier's mobility within DSSCs. Physical evaluations of the microstructure, morphology, contact angle, roughness, electrical, and optical features of PAni-based composite DSSCs were conducted in along with an evaluation of their J–V variables. Continued improvements in DSSC technology and its integration into energy systems will help to create a more sustainable and resilient energy future.

## Materials and methods

### PZ composite CE preparations

*ZnO NPs synthesis*

Using 20 mL of distilled water (DW), 3g of zinc nitrate hexahydrate ($Zn[NO_3]_2{\cdot}6H_2O$) was dissolved to create ZnO NPs. Meanwhile, 20 mL of DW was used to dissolve 4g of sodium hydroxide (NaOH)s. The following step involved mixing an aqueous solution of 5 mol/L $Zn[NO_3]_2.6H_2O$ and 5 mol/L NaOH with magnetic stirring for 2 h at 900 rpm. The resulting mixture was then transferred into a Teflon autoclave and heated for 8 h at 75 °C. The growth of ZnO NPs was indicated by the change from a clear mixture to an opaque medium. The last drying step was finished in a vacuum-sealed electric oven at 65 °C for 24h resulting in finer ZnO nanopowders.

*Synthesis of PAni*

One of the most efficient and crucial methods for PAni production is the in-situ chemical oxidative polymerization methodology described below (see Fig. 1). Whereas the aniline monomer ($C_6H_5NH_2$, Merck, 99.5%) polymerized using hydrochloric acid (HCl, Sigma-Aldrich, 37.0%) as a catalyst and ammonium persulfate (APS) ($[NH_4]_2S_2O8$, Sigma-Aldrich, 98.0%) as a strong oxidizing agent. Using a magnetic stirrer and an ice bath, 0.01

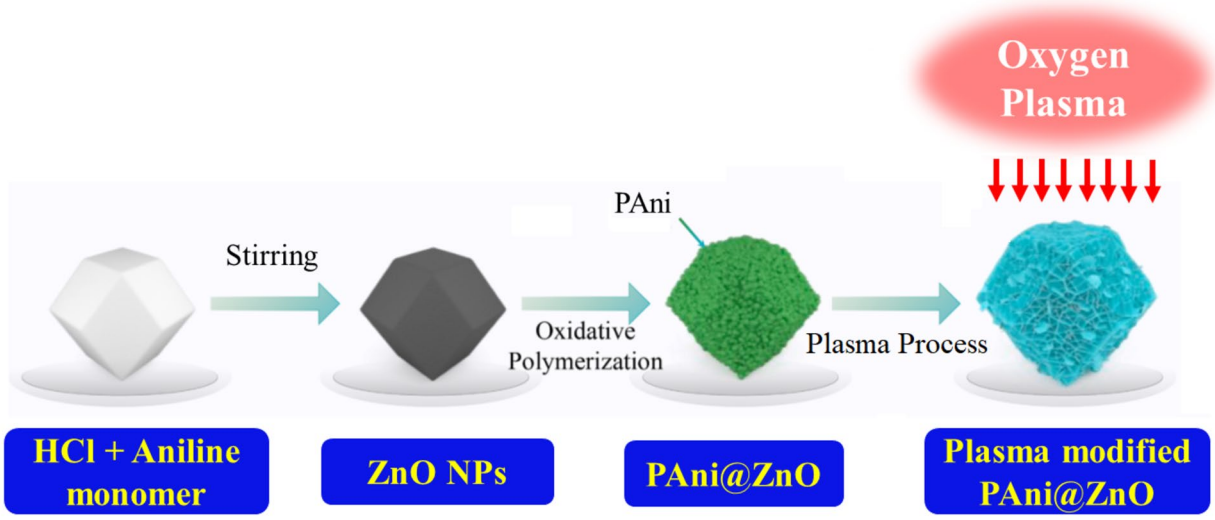


**Figure 1.** Schematic depiction of the PZ composite synthesis and modification process.

mol of HCl and 0.01 mol of APS were diluted separately in 60 mL of DW and chilled to 5 °C. Following that, 0.01 mol of aniline solution was stirred for 30 min in precooled acidic solution of HCl. To prevent a significant rise in temperature while adding the APS solution to the HCl-aniline mixture, it was blended in slowly (drop/drop) with continuous stirring for 5.5 h[21]. During that time, the aforementioned mixture was maintained in an ice bath to preserve a 2 to 4 °C temperature range. The solution started out brownish after a few drops of the APS liquid were added, however as it was thoroughly mixed, it turned dark green with precipitation.

*Synthesis of PZ nanocomposites*

A core–shell structure is formed by physicochemical interaction of ZnO as a core surrounding by a conductive PAni as a shell. ZnO nanopowders were introduced in a beaker containing aniline mixture and stirred with a magnetic stirrer for 2 h to form the PZ composite (see Fig. 1). The essential ZnO solution was ultrasonicated for several minutes after being combined with a 20% vs. 80% aniline solution. Afterwards, in-situ polymerization was accomplished by dropping the diluted APS solution dropwise to the aniline solution at 4 °C for 5.5 h. Within this time, the ice must be replaced 2–3 times to keep it at the proper temperature. The remaining polymerization step was the same as in the PAni synthesis ("Synthesis of PAni" section)[22,23]. The aggregation of ZnO is weakened via the chemical reaction among the hydroxyl and ether groups on the ZnO surface with the $H_2$ of the PAni chain bond. The ZnO NPs were then appropriately dispersed by the aniline solvent. During the polymerization procedures, ZnO and PAni develop a stronger molecular correspond than the $H_2$ bond that forms within the ZnO shell and the hydroxyl group of ethanol[24].

## Plasma modification of PZ CEs

Using a plasma enhanced chemical vapour deposition (PECVD) technique (OTF-1200X-50-4CLV-PE), the resultant PZ composites were exposed to oxygen plasma modification (see Fig. 1). The components were placed in a crucible before being positioned in the center of the maintained temperature area (200 mm length). Following that, using a mechanical pump (EQ-VBS-M1-LD), this tube was evacuated to a starting point of $2 \times 10^{-3}$ mTorr as measured by a Pirani capacitance diaphragm gauge (EQ-PGC-554) before commencing the oxygen plasma glowing. 90 sccm of $O_2$ gas was subsequently introduced into the evacuated chamber at an operating pressure of $0.1 \times 10^{-3}$ mTorr. As well, the plasma discharge was generated by a controlled RF (RF-600-LD) generator with a frequency of 13.56 MHz $\pm$ 0.005% within an adaptable combining circuit with a constant running power of 100 W $\pm$ 1%. The suggested PZ combinations received treatments by varying plasma levels for 0, 2, 4, 4, 6, 8 and 10 min at a processing power of 100 W. Table 1 summarizes the description assignments for pristine and treated PZ CEs at varied plasma levels. The recorded rate of heating was influenced by the plasma runtime from 56 to 69 °C as measured utilizing a temperature controller (EQ-MTS02). Finally, after 10 min of bombardment with oxygen plasma fragments in the reactor tube, the material was allowed to gradually cool to ambient temperature.

## Fabrication of DSSCs systems

A liquid electrolyte was positioned between a modified-PAni composite CE and a $TiO_2$/rGO photoanode in order to manufacture DSSCs, as seen in Fig. 2. The photoanodes were designed of rGO/$TiO_2$ hybrids with 50 wt% $TiO_2$ NPs and a little quantity of rGO (50 wt%). Highly effective rGO nanosheets were synthesised using a modified Hummer's process, whereas anatase $TiO_2$ NPs were produced using a hydrothermal autoclave technique, as described in detail in our previous studies[25,26]. The FTO coated conducting substrates ($2 \times 2$ cm$^2$) were cleaned using (0.1 M) HCL in methanol for 5 min in an ultrasonic bath before being formed into DSSCs. The cleaning procedure involved rinsing the glass surfaces with detergent (5 wt%) and distilled water (DW). Following several

| Labelled | Description |
|---|---|
| PZ0 | PAni–ZnO (0 min) |
| PZ2 | PAni–ZnO (2 min) |
| PZ4 | PAni–ZnO (4 min) |
| PZ6 | PAni–ZnO (6 min) |
| PZ8 | PAni–ZnO (8 min) |
| PZ10 | PAni–ZnO (10 min) |

**Table 1.** Description assignments for pristine and treated PZ CEs with different plasma doses.

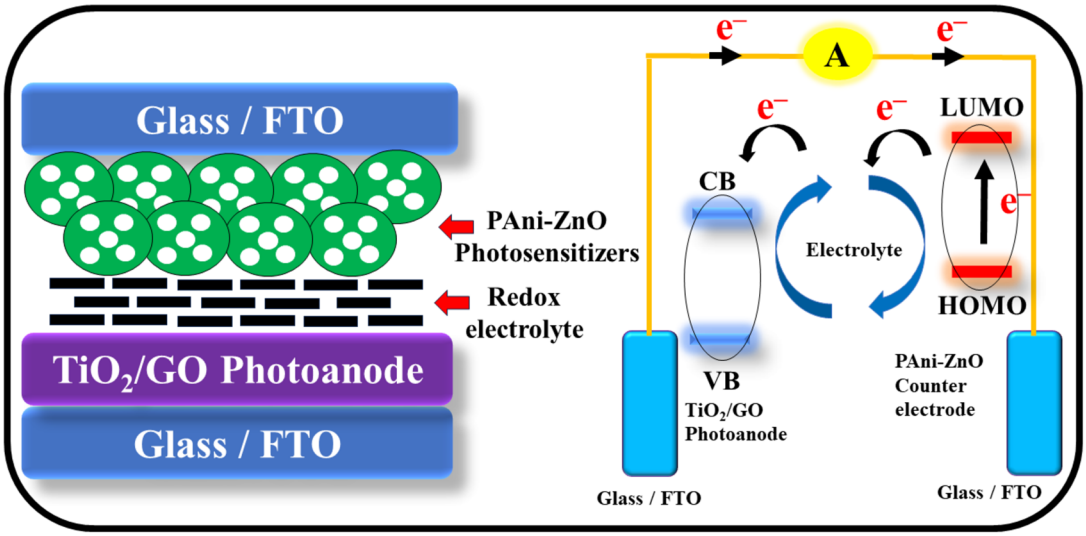


**Figure 2.** Schematic device construction and operating mechanism of DSSCs.

minutes of soaking in DW and washing with ethanol, the FTO glass plates were sonicated. The above procedure was done three times to ensure that no organic contaminants remained in the FTO plates. The proposed rGO/$TiO_2$ composites were dissolved in distilled water before being spin-coated (VTC-50A) onto conductive FTO substrates at 1200 rpm for 2 min. To create CEs, clean FTO glass plates were soaked in the aforementioned PAni complex solutions for 1 h at 80 °C. The thicknesses of the deposited CEs were regulated (200–250 nm) according to a predetermined technique using a thin-film measurement device (EQ-TFMS-LD). Finally, DSSCs were assembled with a rGO/$TiO_2$ thin film as the photoanode, an electrolyte solution, and pristine and treated PZ at varied plasma dosages (2, 4, 6, 8, and 10 min) as CEs.

## Instruments used

The effect of plasma on the formation of the functional groups in doped PAni composites was examined using Fourier Transform Infrared (FTIR Jasco 4100_Japan) Spectroscopy, which operates in the 4000–400 $cm^{-1}$ range. Meanwhile, X-ray diffraction patterns (XRD) were recorded using a Bruker D8 ADVANCE diffractometer using CuK radiation in the 10°–80° range. Besides, the morphology of the formed composites was analyzed by scanning electron microscopy (SEM JSM-5500, JEOL_Japan). Furthermore, physical investigations of bulk density and apparent porosity received using the Archimedes approach. The contact angle, wet energy, spreading coefficient, and work of adhesion were all recorded with a contact angle instrument (SEO Phoenix 300). As well, the surface roughness was determined utilizing a Talysurf 50-Taylor Hopson Precision profilometer. Moreover, the resistivity tester with a four-point probe (4PP EQ-JX2008-LD) was used to measure the electrical resistance. Each PAni composite's average electrical resistance was estimated utilizing data from more than 10 different locations. Optical assessments were performed using a UV–Vis spectrophotometer (SPECORD 200 PLUS, analytical Jena) within an emission wavelength ranging from 190 to 1100 nm. In addition, a solar simulator system was used to assess the cells' J-V characteristics under standard light conditions of 1.0 Sun at 25 °C. Regarding electrochemical impedance spectroscopy (EIS) experiments, symmetrical cells were developed with identical CEs as well as soaked in redox electrolyte. EIS of the dummy cells was conducted within 100 Hz and 100 kHz. Enlitech QE-R system, which is outfitted with a 75W xenon arc lamp source, was employed to evaluate the wavelength-dependent incident photon-to-current conversion efficiency (IPCE). The simulated test was carried out with a KEITHLEY 2400 Source Meter & a 100 W ozone-free Xenon lamp as a light source under calibrated conditions (AM 1.5 filter, 100 $mW/cm^2$).

## Results and discussions

### FTIR spectra

The FTIR spectra of the ZnO-containing synthesized PAni composite, both before and after it was exposed to varying degrees of plasma modification, were presented in Fig. 3. While Table 2 enumerated the subsequent distinctive bands of modified-PZ specimens: The N–H stretching band first occurred between 3570 and 3004 $cm^{-1}$, then the C–H stretching of $CH_3$ and $CH_2$ regarding 2900 and 2800 $cm^{-1}$, respectively[12]. The C=N stretching of the quinonoid ring happened at 1656 $cm^{-1}$ and 1711 $cm^{-1}$ for virgin PZ0, whereas evolved at 1685 $cm^{-1}$ and 1738 $cm^{-1}$ for processed compounds. Meanwhile, the intensity declined while the input signals switched to higher wavenumbers for the processed combinations, evidenced in Fig. 3. Following that, the C=C stretching of the quinoid ring formed between 1605 and 1482 $cm^{-1}$ in each specimen[27]. A band about 1400 $cm^{-1}$ was recognized as a C–$N^+$ stretching vibration, while the band's intensity rose for PZ that received modification. Only in the reacting

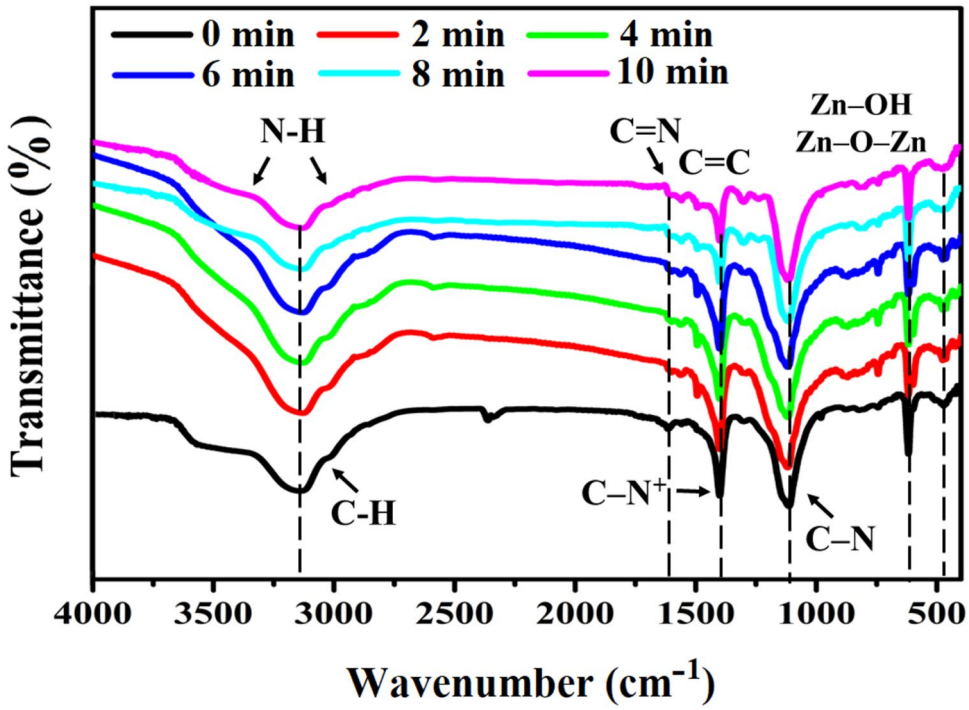


**Figure 3.** FTIR spectra of modified-PZ CEs depending on the oxygen plasma levels.

| Chemical bonds | Wavenumber ($cm^{-1}$) |
|---|---|
| N–H stretching | 3472–3028 |
| C–H of $CH_3$ | 2936 |
| C–H of $CH_2$ | 2865 |
| C=N stretching of quinoid ring | 1685 decreased |
| C=C stretching of quinoid ring | 1586–1478 |
| C–$N^+$ stretching vibrations | 1404 |
| C–N stretching of aromatic ring | 1302 |
| C–N stretching of primary amine | 1238 |
| C–N stretching in benzoid ring | 1144 |
| C–H In-plane bending | 1115 |
| –$NH^+$– benzoid ring stretching | 1031 |
| C–H out of plane bending | 983 |
| Meta substitutions, 1,3 disubstitution in benzene ring | 880 |
| Para substitutions, 1,4 disubstitution in benzene ring | 803 |
| Ortho substitutions, 1,2 disubstitution in benzene ring | 741 |
| Aryl nitro compounds | 618 |
| ZnO | 461 |

**Table 2.** The assignment of FTIR spectra of pristine and treated PZ CEs at varying plasma dosages.

composites, performed the predominant amine and aromatic ring's C–N stretching manifest at around 1300 $cm^{-1}$. The benzoid ring exhibited C–N stretching at 1140 $cm^{-1}$, whereas Zn–OH, Zn–O–Zn bond, and free oxides were represented by peaks at 740 $cm^{-1}$, 616 $cm^{-1}$, and 472 $cm^{-1}$, respectively. Likewise in processed specimens the protonated $–NH^{+}–$ benzoid ring stretching was observed at 1050 $cm^{-1}$, indicating that the synthesized PAni was emeraldine based. Therefore, oxygen plasma modified the PAni structure, converting it into emeraldine salt[28].

## XRD study

The PZ hybrid structural modifications carried on by varied intervals of $O_2$-plasma treatment (0, 2, 4, 6, 8 and 10 min) were investigated using the XRD technique. Whereas, XRD profile peaks of as-produced PZ composites in the (10°–80°), (22°–24°) and (34.5°–36.5°) ranges were depicted in Fig. 4a–c, respectively. No splits were seen inside any of the compositional peak's peaks with a rise in the plasma activity. The discovered peaks of ZnO in this study are well matched with JCPDS card no. 36-1451, indicating that the material crystallizes in a typical wurtzite hexagonal structure[29]. This nanofiller is additionally associated to the corresponded to plans of (100), (002), (101), (102), (110), (103) and (112) that are situated at 32.45°, 35.44°, 37.26°, 47.98°, 54.86°, 62.43° and 67.28°, respectively. Meanwhile, the notable peaks located at 17.53°, 23.21°, 26.01°, 35.44°, 47.98°, and 54.86° might be indexed as (110), (012), (003), (221), (102), and (323) facets, respectively, correspond very well with orthorhombic crystalline PAni (JCPDS, Card no 053-1890)[30]. It is notable that all of the aforementioned peaks of the $O_2$ plasma-modified PZ compounds remained unchanged following modification as seen in Fig. 4, indicating that all of the peaks possessed the identical phase structure. Therefore, exposure to $O_2$-plasma ions at various levels indicates these ions have successfully interacted with the PZ system. However, it is obvious that the modification level of composites has a major impact on their crystalline nature along with peak intensity, which gets enhanced as treatment time rises. Additionally, the plasma species assisted in the creation of new peaks at 35.44° and 47.98° that substituted the PAni and ZnO peaks and grew rapidly as the plasma dosage rose. Those revealed peaks suggested that PZ composites formed with regard to the plasma modification level and increased matrix crystallinity. Such deformation of the structure may be carried on by fluctuations in the host PZ matrix's inter-planar spacing, lattice properties, defects level, and crystallite size[31]. Moreover, as the processing intervals grow, all of the peaks in Fig. 4a slowly shift to a higher diffraction angle as compared to the pristine PZ composition. In this case, zoomed images of the main PAni peak at $2\theta = 23.21°$ and the co-peak at $2\theta = 35.44°$ clearly highlight this shifting pattern (see Fig. 4b,c). Whereas, main PAni peak generated by parallel and consistently spaced-apart polymer chains, that result in crystalline regions bordered by amorphous areas[32]. According to these results, $O_2$ ions are equally distributed inside the lattice structure, as well as variations in high-energetic ion concentration have relatively little influence on physicochemical processes and composite structure[31]. In this regard, crystalline conducting polymer compounds are particularly appealing in the manufacture of solar cells given their better hole mobility.

Along these lines, the crystallite size and degree of crystallinity of the treated PZ compounds enhanced as compared to pristine sample, as displayed in Fig. 5. The Debye–Scherrer formula was employed for estimating the crystallite size[33]. As modification time rises, crystallite size tends to grow till PZ8 before dropping towards PZ10 specimen as a result of ionic interaction between $O_2$ ions and hydroxyl groups. In a similar vein the crystallinity

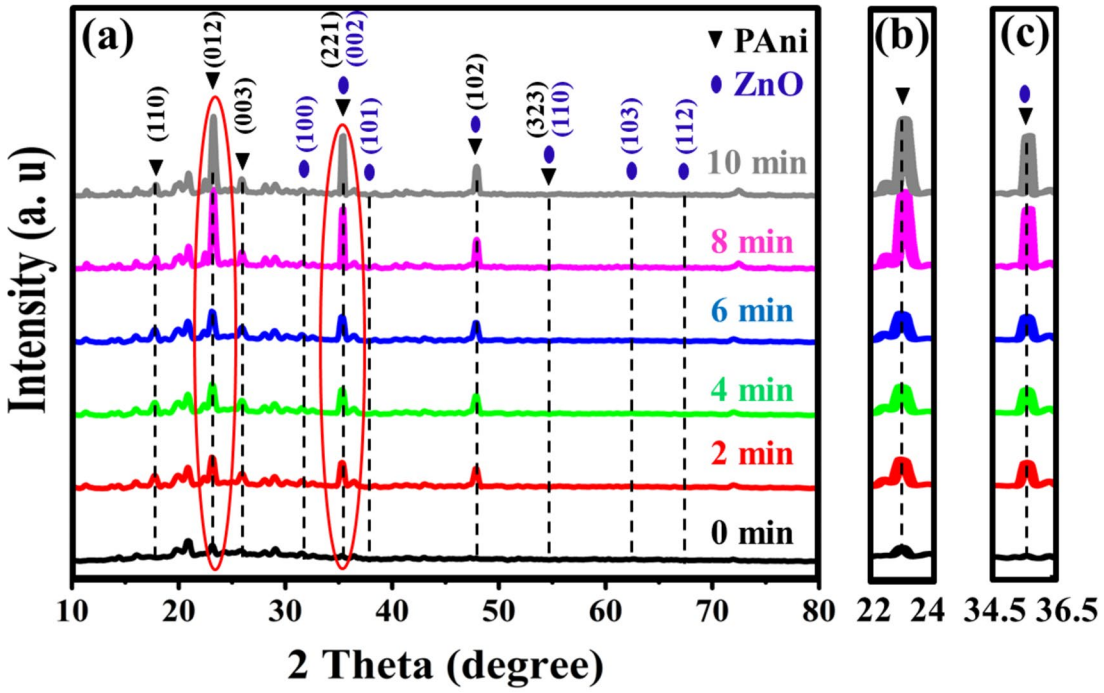


**Figure 4.** XRD patterns of PZ composites exposed to $O_2$-plasma at various times.

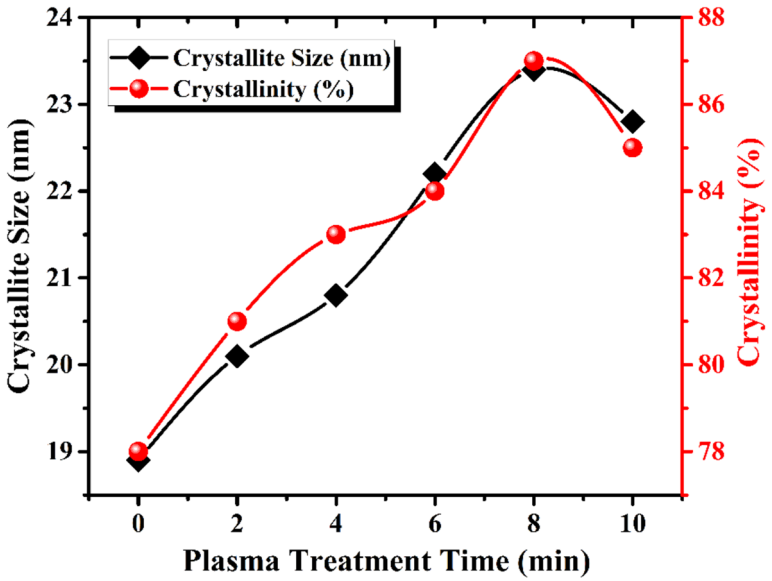


**Figure 5.** Crystal size and crystallinity of modified-PZ compounds via different plasma levels.

trend matches to a crystallite size expansion of the hybrid systems, with an optimal value of 87% as the level of included $O_2$ ions grows to 8 min. However, PZ10 possessed a decrease in crystallinity degree when the treatment dose was raised further. These findings indicate that oxygen ions are well distributed inside the PAni lattice structure and that ion concentration variations have limited influence on the composite structure[31]. Several prior investigations have demonstrated comparable behaviours of PZ substances[34,35].

## Morphology

SEM images and pore size distributions of pure and treated PZ compounds with varied plasma modification levels are displayed in Fig. 6. Meanwhile, this wide range of plasma-ions created a variety of morphological properties in PAni blends. Figure 6a details the surface characteristics of pristine composite, which included fine gaps, wrinkled, and crumbly structures. In order to prevent excessive restacking and agglomeration of embodied ZnO NPs, this PAni characteristic is essential[36,37]. This non-agglomerated filling emerged about by well-integrated ZnO NPs within the PAni lattice, that may be interpreted via the development of the PAni shell on the metal oxides' surface. By generating repelling forces between the components, this tendency prevents their accumulation[38–40]. Following exposure to various $O_2$ plasma bombardment levels, its morphological nature modified often. However, this surface amorphous vanished into more symmetrical forms, these were depicted as a scattering of needles with a few stacks, as in Fig. 6b–d. Subsequently, at more intense plasma modification levels (8, 10 min), the structure of the composites likewise grew, exposing a fully columnar structure with more fine-pores, multiple bonds, and heightened internal energy[41]. The aforementioned morphological phenomenon could be owing to the infusion of sufficient energy during the plasma ions modification, which optimizes both the ZnO functional groups and the PAni matrix, since they assist in creating hydrogen bonds and so adhere better to one another[42]. In this vein, plasma collisions have gotten better the mixing of blends with $O_2$ ions, that may affect the film's morphology and quality and modify the sequence of polymer chains. Higher light absorption and charge transfer inside the solar cell can result from an optimized morphology.

The average pore sizes of the PZ composites were additionally statistically evaluated according to the treatment level. Despite the average pore size for the pristine state was assessed to be 0.127 µm, it was raised to 0.167 µm via the plasma treatment for 2 min. Afterwards, the size values then gradually grew with raising the level of modification, reaching an optimal size of 0.27 µm after 8 min of immersing the PZ composite in the $O_2$ plasma environment. However, exceeding the plasma treatment time by 10 min resulted in the opposite pattern, with the estimated value decreasing to 0.138 µm. These findings could be clarified through the formation of novel bonds of hydrogen among ZnO and PAni–$H_2O$ and intermolecular covalent bonds as a consequence of $O_2$ plasma species bombardment[43,44]. These linkages affect the pace at which hydration nanocrystals develop and allow ions and nanofillers to disperse uniformly along PAni chains[26,45]. The miscibility of the nanofiller resulted in a noticeable enhancement in the electrical properties and surface roughness of these compounds.

## Porosity and bulk density of CE martials

Given the significance of porosity, and thus in accordance with the aforementioned, the apparent porosity and density parameters of the produced composites were determined using the Archimedes approach (see Fig. 7). As their presence is among the key elements affecting CE conductivity. The molecule known as Pristine CE experienced a smallest apparent porosity rate (21%), then proceeded on to rise to 33, 39, 44, and 51% at the 2, 4, 6, and 8-min plasma dosing levels, respectively. However, the tendency was reversed with increased $O_2$ plasma species dopants, as seen by the apparent porosity at the CE-10 min specimen dropping to 47%. As shown in

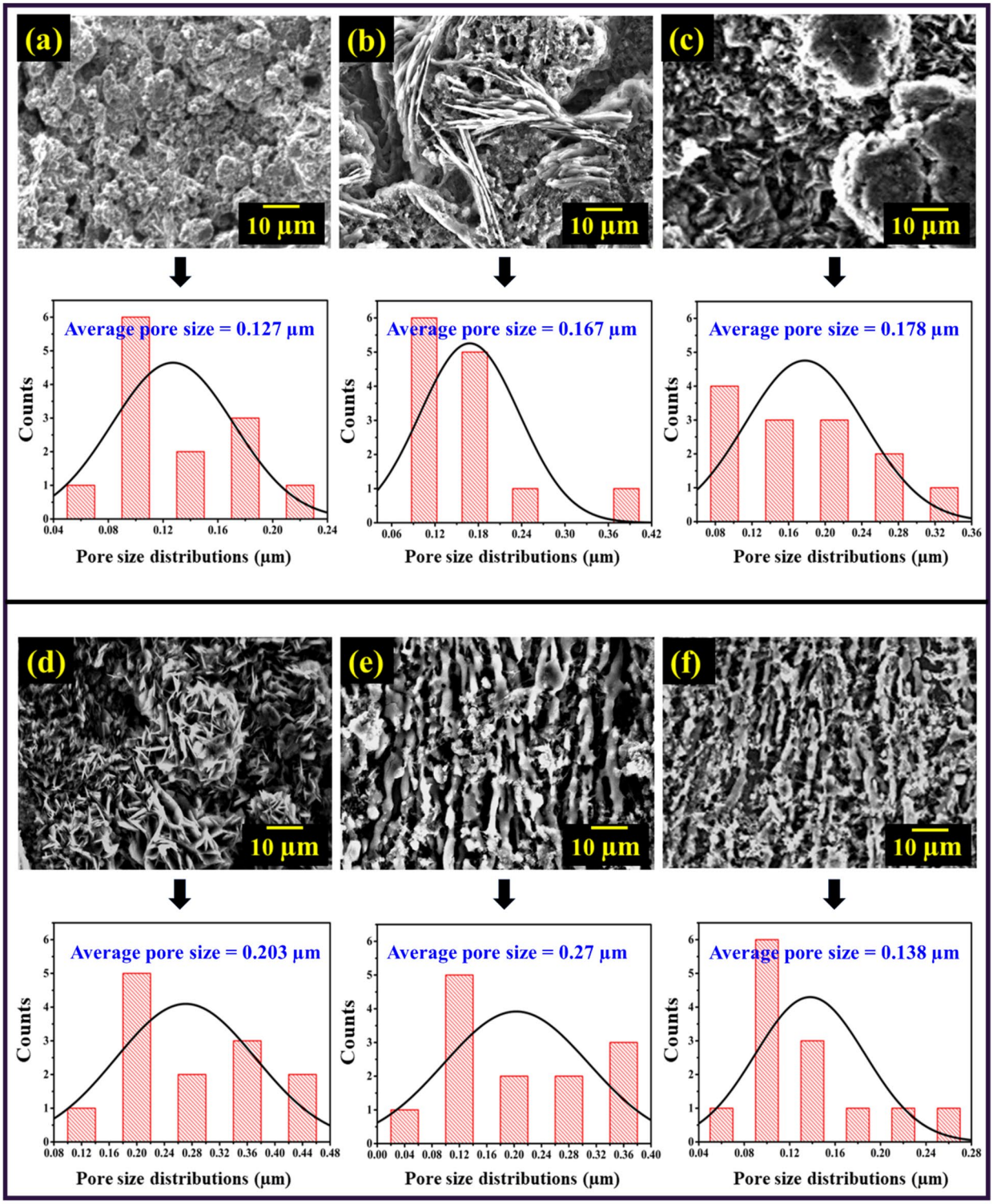


**Figure 6.** SEM micrographs and pore size distribution of PZ hybrids processed at various plasma times: (**a**) t = 0 min, (**b**) t = 2 min, (**c**) t = 4 min, (**d**) t = 6 min, (**e**) t = 8 min and (**f**) t = 10 min.

Fig. 7a, the fluctuation in the aforementioned pattern is strongly associated with the mean pores value derived from SEM micrographs. Exposing CE to a plasma environment for 8 min is obviously the most suitable level to improve the apparent porosity needed to be an effective electrical conductor. CE materials that have received plasma exhibit higher porosity than pristine one. The reason for this is related to the fluctuation in the amount of C=N and C=C quinoid rings, as well as the formation of a new protonated $-NH^{+}-$ benzoid, ending in excellent adherence of injected $O_2$ plasma species or pores[27].

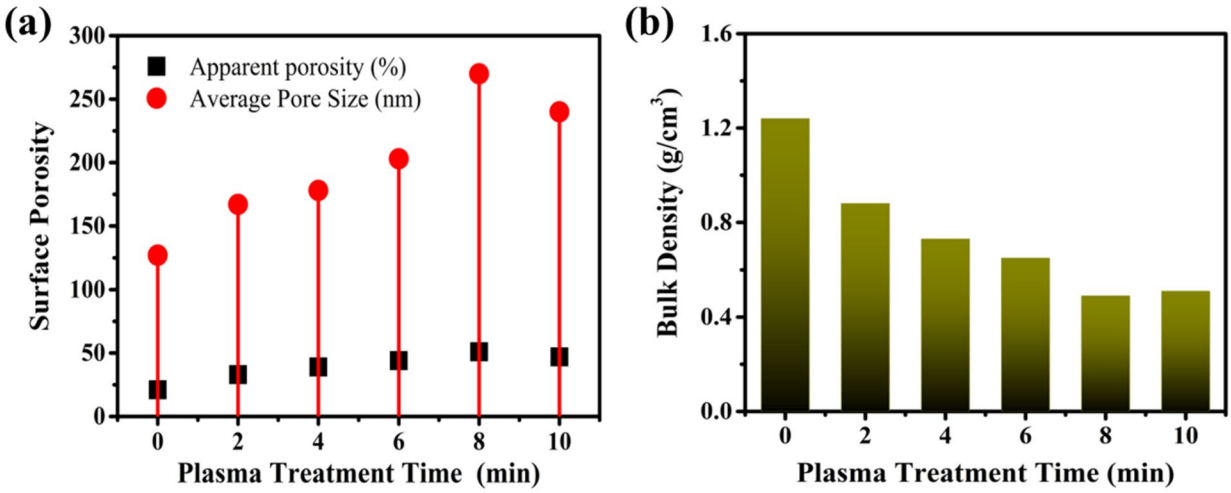


**Figure 7.** (**a**) Porosity, (**n**) Bulk density of CE martials with respect to plasma level.

In general, pure PAni possesses a bulk density of 1.4–1.6 g/cm$^3$, while ZnO exhibits a density around 5.61 g/cm$^3$[46]. Whenever both of these substances combine to produce a blend, the density is determined by the relative amounts of PAni and ZnO, as well as any vacant areas or further inclusions like a plasma injection. As indicated in Fig. 7b, the bulk density of the pristine CE substance was 1.24 g/cm$^3$, which was lowered to 0.88, 0.73, 0.65, and 0.49 g/cm$^3$ at $O_2$ plasma treatment levels of 2, 4, 6, and 8 min, respectively, while growing to 0.51 g/cm$^3$ for 10-min-CE materials. These results are corroborated by the differ-dense microstructure shown in the SEM pictures. Further, the formation of finer particles is responsible for the fluctuations in the density pattern. Denser microstructures are the result of increased atomic diffusion rates, which drive densification[47,48]. Besides, the tendency of the compounds to degrade throughout the treatment cycle results in a decrease in the density of modified composites. Prior to then, research using a variety of dopants, including poly (L-lactic acid)/polyaniline/p-toluene sulfonic acid (PLLA/PAni/TSA), and polyvinyl alcohol/polyaniline/silver (PVA/PAni/Ag) composites, showed a comparable bulk density behaviour profile[46,49].

## Contact angle measurements

The bombardment of activated ions emitted by concentrated plasma exhibited a significant influence on the surface energy and active parts of the treated PAni chains. This impact was reflected in the effectiveness of hydrophilic and hydrophobic sites. Figure 8a–d depicts the surface characteristics of PZ0, PZ2, PZ4, PZ6, PZ8 and PZ10 composites, including contact angles (CAs), adhesion force, wettability, and water droplet spreading coefficient. The CA of the pristine PZ was 59.7° and systematically reduced to 19.4° in PZ8 with the continuously increasing plasma treatment doses, before growing in PZ5 (22.6°) compound. This trend of enhancement following oxygen plasma usage at $t \leq 8$ min, indicates the redistribution of hydrophilic active zones on the surfaces of the treated composites rapidly grows. These discoveries additionally correspond to the distinctive chemical reactions on the outer layer of composites generated by collisions of high-energy $O_2$ plasma species, resulting in the creation of novel defects in PZ compositions including vacancies, O–H, and C–H groups[50]. Since the CA value was declining, the adhesion action rabidly rose in an inverse trend to reach a peak value of 141.2 mN/m at the PZ8 composition, depicted in Fig. 8b. Meanwhile, the wettability and diffusion coefficient were both substantially influenced by the oxygen plasma dosage level as observed in Fig. 8c,d. This is consistent with the fact that narrower angles between rough surfaces match to reduced shrinkage[51]. Furthermore, the vertical topographic variation (porosity) induced by plasma species additionally influences the physicochemical performance, surface charge density as well as electrochemical features of PZ surfaces[52–55]. Pereira and et al.[56], reported the similar behaviour on PAni-based nanocomposite films[56].

## Roughness, electrical and optical measurements

After $O_2$ plasma exposure, the bombardment of energetic ions and rapid electrons exhibited a substantial influence on the surface energy as well as the interior structure of PZ compounds[20]. This effect may be intensified further by transitioning to a rougher surface nature in addition improving the electrical characteristics of the treated materials. The surface roughness features (i.e., average roughness, Ra) and electrical performance (i.e., electrical conductivity) of the pristine and treated PZ blends were clarified in detail in Fig. 9a,b, respectively. The pristine composite's surface roughness parameter, Ra, increased with regard to the oxygen plasma level, peaking at 7.21 µm with PZ8 and declining to 6.77 µm with PZ10, depicted in Fig. 9a. These variables were related to plasma processes as they contribute to the formation of a more types of hills and valleys, which are reflected in an increase in PZ compound surface wrinkling[57]. In addition, since powdered material adhered to component surfaces more effectively when partially melting, the heat absorbed inside an oxygen plasma environment had an impact on the creation of the thin-walled structures, boosting surface roughness as a result[58].

According to Fig. 9b, electrical conductivity responded similarly to roughness, beginning at PZ0 with a value of 7.12 S/m rapidly rising to its the peak value at PZ8 (10.25 S/m). However, raising the oxygen plasma doses to

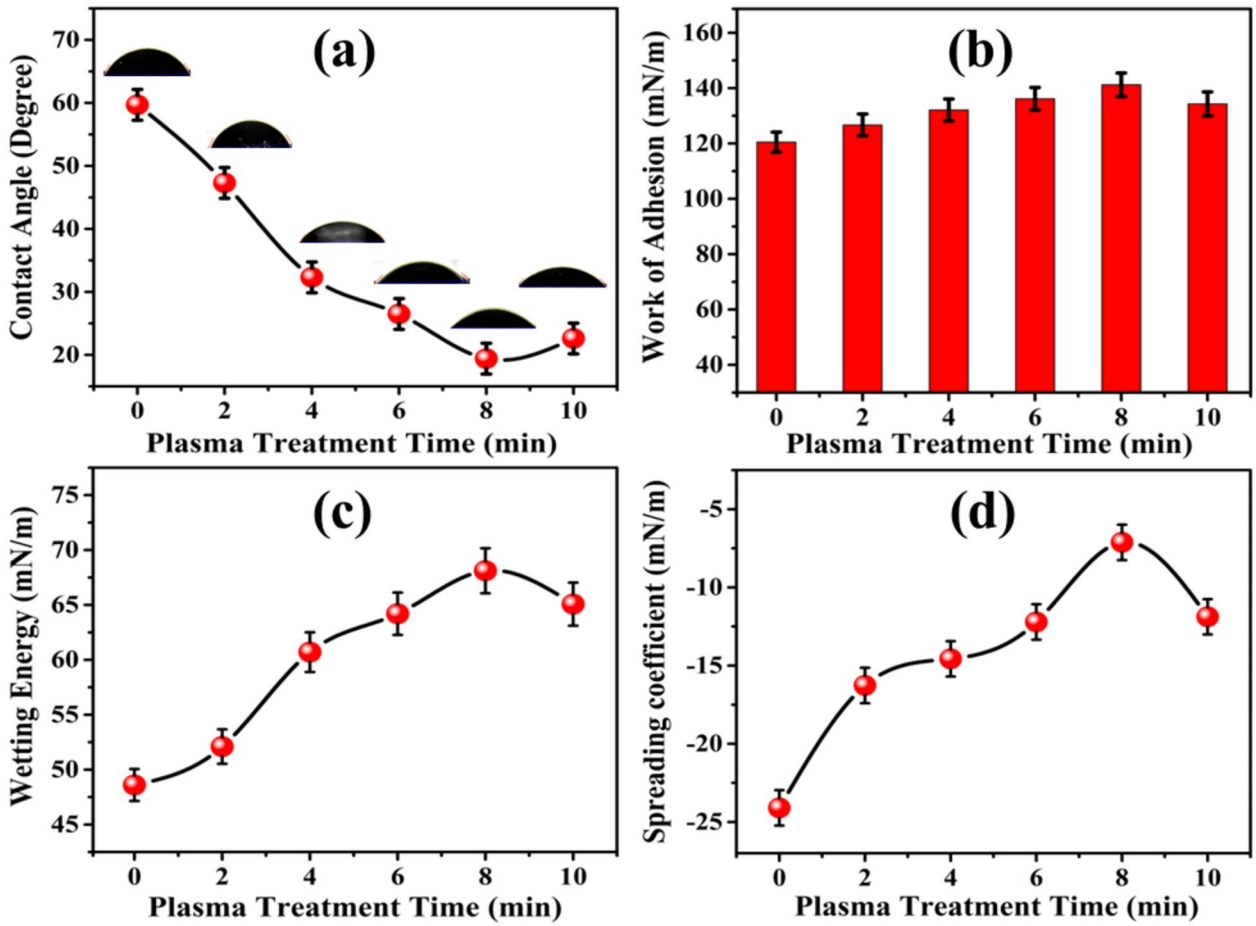


**Figure 8.** (**a**) Contact angle, (**b**) work of adhesion, (**c**) wetting energy and (**d**) spreading coefficient curves of PZ compounds at various processing times in a plasma environment.

PZ10 reduced the conductivity to 9.86 S/m. One of the aspects responsible for this behavior is the formation of physicochemical reactions during plasma treatments between ZnO NPs contained within the matrix structure, resulting in a modification in the oxidation state of the molecular structure[59]. Basically, there are a number of strategies implemented to boost a polymer's electrical conductance: pairing and π–π stacking, annealing, stretching, or additional post-treatment ways to help align chains of polymers as well as improve charge transport; chemical structure modification and thickness control; and optimization of synthesis requirements[56,59,60]. In light of this, the oxygen plasma treatments caused considerable improvements in the electronic defects, such as oxygen vacancies, for PAni-modified substances[36]. Changes in the oxidation level of PAni are also expected to influence its electronic structure[60]. Besides, increasing the conjugation length in the polymer backbone and improving π–π stacking interactions between polymer chains promote electron mobility. Thus, it assisted to boost charge carrier mobility from the polar $O^{2-}$ ZnO surfaces along polymer chains[61]. However, keeping the exposure duration to relatively long intervals (10 min) resulted in a drop in conductivity, as the segregation effect between PAni chains grew substantially with extended treating, resulting in high ZnO agglomeration inside the PAni matrix. Due to this, a non-conductive agglomeration zone forms in the PZ layer, reducing carriers mobility and the ability to conduct electricity[37].

Figure 9c depicts the absorbance profiles in the wavelength between 300 and 800 nm for both pristine and processed CE compounds via various plasma dosages. While the absorbance levels of each of the modified CEs varied somewhat, they all showed comparable absorption behaviour. The unmodified material has a wide peak for absorbance in the range of 335–600 nm, while the plasma level rises, its depth gradually declines. Additionally, a further proportionate absorption inclination in the same region of the absorption pattern is prompted by the longer plasma lifetime, indicating a higher absorption of visible spectrum illumination[62]. Until then, another effect of up to 8 min of plasma exposure duration on CE composite surfaces is shifts towards smaller wavelengths in the received wavelengths between 550 and 750 nm. This change highlights how energetic plasma species affect ZnO NPs' electronic structure in the valence band, where they may interact with the PAni's higher occupied molecular orbital (HOMO)[24]. However, if the duration of processing is extended to 10 min, the response varies and there is a little shift towards longer wavelengths, supporting the creation of the ZnO hybrid[63]. For further details, consider pristine materials as an energy absorption comparable at wavelengths of 330, 420, and 600–800 nm, resulting in the transitions $\pi \rightarrow$ polaron excitonic of the quinoid rings, $\pi \rightarrow \pi^*$ inside the benzenoid rings, and Polaron $\rightarrow \pi^*$ of the quinoid rings, respectively[64]. Likewise pristine CE possesses a peak at 690 nm, that

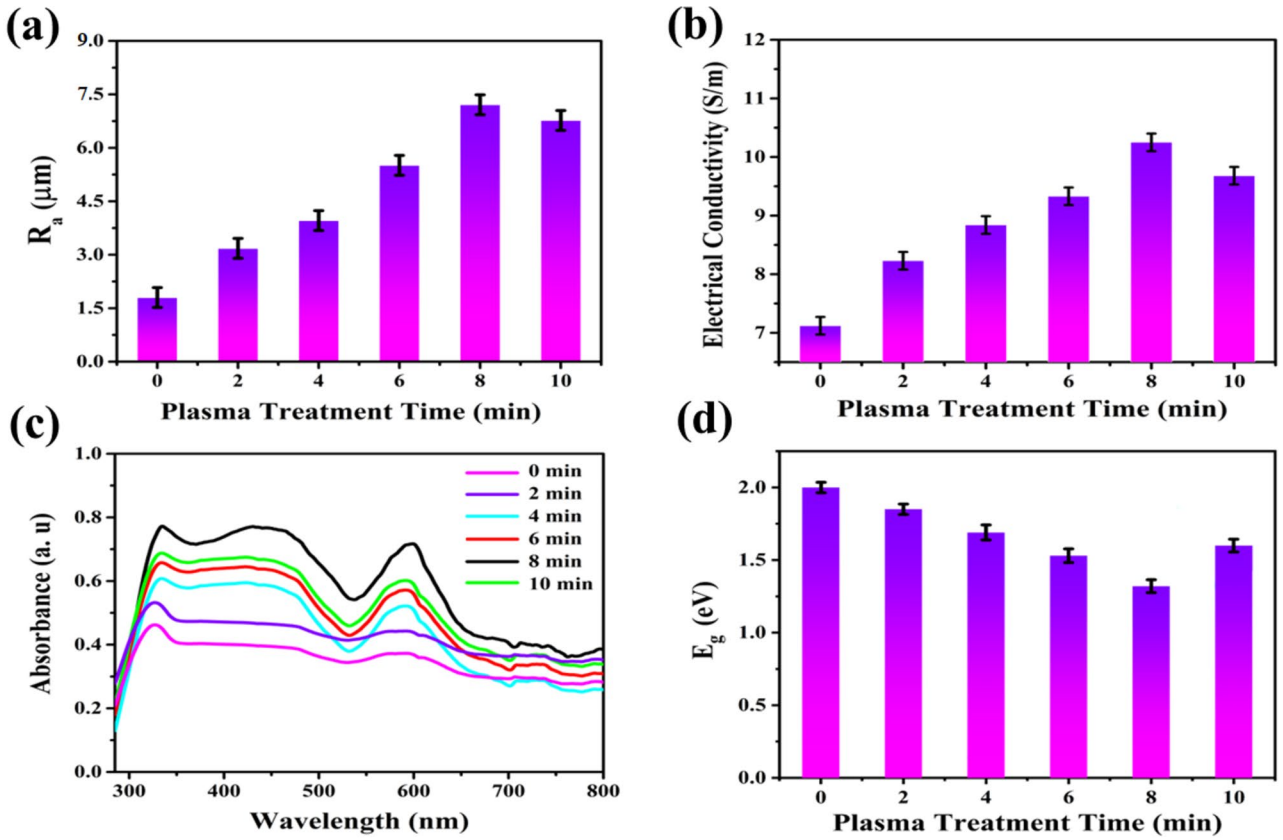


**Figure 9.** (**a**) Surface roughness, (**b**) electrical conductivity, (**c**) absorbance, and (**d**) optical band gab of modified PZ composites at varying processing times.

is correlated with the excitonic transition of quinoid and benzenoid compounds. In the composites at issue, these recorded peaks reveal a progressive rise in intensity along with a little movement towards longer wavelengths. The following verifies the existence of the polaron tape formed in the PAni's bandgap and that the addition of $O_2$ ions produced a significant impact on it[65]. Previous observations demonstrated that the PAni-based composites absorption curve exhibits the same tendency[66,67].

In this vein, Tauc's formula[68] was utilized for calculating the energy band gap (Eg) for each molecule, as seen in Fig. 9d. The Eg was 2 eV for the pristine CE, while it declined consistently in relation to the plasma degree, reaching 1.32 eV in the PZ8 CE followed by rising to 1.6 eV in the PZ10 CE. The aforementioned is linked to the $\pi$–$\pi^*$ shift in the UV and the bipolaronic band in the visible regions[67]. Whereas, the amorphous phase's short-range order along with defect state determine the amount of illumination may be absorbed[52,69]. Both an increase in the disorder amount and a decrease in the density of the defect states could possibly be responsible for the current structure's lowering in optical bandwidth. There is a possibility that injecting plasma dopant ions to modify the optical features of a PZ structure could end up in an actively absorbing synthetic materials.

## EIS and IPCE characterizations

EIS tests were carried out to examine the impact of injection plasma ions within PZ structure on the interfacial charge transfer activity of the CEs; the resulting Nyquist plots were displayed in Fig. 10a. Nyquist plots showing the imaginary component (ImZ) versus the real part (ReZ) of the complex impedance (Z = ReZ + ImZ) as a function of frequency. Additionally, the charge transfer resistance ($R_{ct}$) among the liquid electrolyte and CE, as well as the ohmic series resistance ($R_s$) at the interfaces of the FTO/CE composites, were derived by fitting the Nyquist profiles of DSSC impedance data with the equivalent circuit (Inset in Fig. 10a), following the principle described by Bisquert[70]. Whereas, $R_s$ is often represented by the intercept of the semicircle with the real impedance axis, while $R_{ct}$ corresponds to the diameter of the semicircle. Table 3 provides the estimated $R_s$ and $R_{ct}$ of the CEs mentioned.

The inclusion of $O_2$ plasma species to the conducting chains of PAni CE yields a drop in the amount of $R_s$ for all samples, as observed in Table 3, indicating an improvement in the interaction between both the composites and the FTO surface[71]. More details, in regard to the plasma degree, the $R_s$ value declined substantially, reaching an optimal value of 17.6 Ω at CE-8min material. These elements might encourage the injection of additional electrons into ZnO's conduction band[3]. Clearly, following hybridization under the plasma atmosphere, there is rapid interfacial charge transfer circles and superior splitting of charges within the PAni hybrids CE composition versus the pristine CE compound[72]. Nevertheless, with the CE-10min material, the $R_s$ value rose (i.e., 18.9 Ω), implying that further plasma doses may diminish the overall amount of active surface area, which might lead to

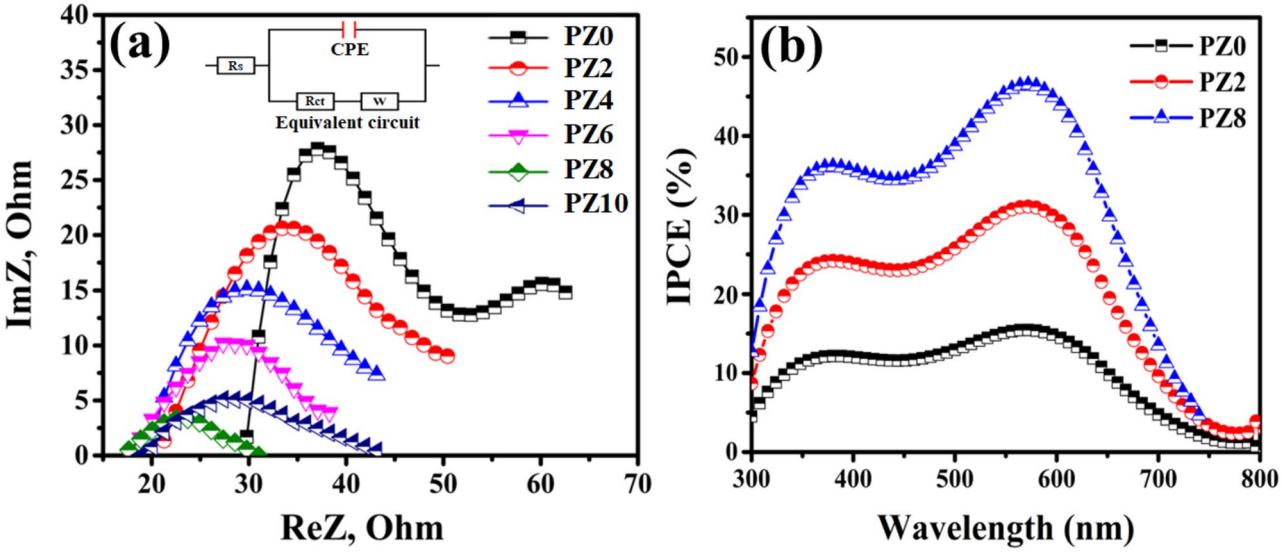


**Figure 10.** (**a**) Electrochemical impedance spectroscopy and equivalent circuit, (**b**) IPCE profiles of DSSCs based on PZ CEs treated with different plasma levels.

| Plasma treated CEs (min) | $V_{oc}$ (V) | $J_{sc}$ (mA/cm²) | FF | η (%) | $R_s$ (Ω) | $R_{ct}$ (Ω) |
|---|---|---|---|---|---|---|
| Pristine | 0.581 | 10.028 ± 0.42 | 0.61 ± 0.02 | 3.554 ± 0.19 | 29.9 | 30.3 |
| PZ2 | 0.587 | 12.706 ± 0.36 | 0.62 ± 0.01 | 4.624 ± 0.21 | 21.3 | 36.4 |
| PZ4 | 0.616 | 14.171 ± 0.30 | 0.62 ± 0.01 | 5.412 ± 0.22 | 20.1 | 34.0 |
| PZ6 | 0.634 | 14.516 ± 0.29 | 0.63 ± 0.01 | 5.798 ± 0.21 | 17.6 | 23.1 |
| PZ8 | 0.640 | 15.616 ± 0.27 | 0.63 ± 0.01 | 6.296 ± 0.29 | 17.6 | 13.4 |
| PZ10 | 0.616 | 14.806 ± 0.30 | 0.62 ± 0.01 | 5.655 ± 0.22 | 18.8 | 24.3 |

**Table 3.** Features of designed DSSCs based on PZ CEs treated with different plasma levels.

a few agglomerations of ZnO NPs in the resulting hybrid[5]. Meanwhile, the derived $R_s$ values of all modified CE compounds are still lower than that of pristine, optimizing DSSCs constructed with CE-8min, indicating possess better charge transfer kinetics between the FTO substrate than that of untreated CE[73]. Similarly, when increasing the plasma doses (i.e., 0, 2, 4, 6, and 8 min), the $R_{ct}$ value gradually drops (i.e., 30.3, 36.4, 34, 23.1, and 13.4 Ω), while it tends to rise of 24.3 Ω when the plasma doping level reaches CE-10min. Reduced active sites for storing liquid electrolyte can be caused by a significant quantity of plasma modification for 10 min. The aforementioned may contribute to a drop in the interaction within the CE substance and the electrolyte, therefore reducing the process of redox reactions ($I_3^-$ reduction to $I^-$)[74]. Therefore, it can be concluded that an 8-min exposure to CE material is adequate to provide the best possible conditions for the CE blend structure. More notably, compared to pristine CE, CE-8min compound revealed reduced $R_{ct}$, suggesting superior charge transfer kinetics[75].

As a general rule, photocurrent density in DSSCs is mainly dictated by the initially photoexcited electron number, the electron injection performance via dye to semiconductor, as well as the amount of recombination among the injected electrons and the oxidized or redox sequence in the electrolyte[76]. Herein, a number of intricate aspects are taken into account, the increase in photocurrent density renders sense. First, there is a chance that a high charge separation efficiency will be induced by the hybrid effect combining ZnO and PAni in the plasma atmosphere's evolution[77]. Energetic plasm radicals hold the potential to enhance the chemical stability of the CE core–shell. This could impede the development of the dye/$Zn^{2+}$ interaction on the ZnO surface, hence potentially speeding up the electron injection process via dye molecules toward semiconductors. Third, both the dye and ZnO's energy levels and gaps are compatible with those of PAni[78]. When the dye captures light and produces photoexcited electrons, the modified-CE layer may quickly transport those electrons into ZnO's conduction band, thereby enhancing the metal's electron density. Additionally, the novel core–shell structure may hinder the electron reverse transfer reaction. Given the rate at which recombination occurs and the dye properties assumed, it makes sense to suggest that the injected electrons could have a significant role when assessing how well the DSSC constructed with various modified CEs performs. These findings verify that one of the main factors enhancing the photovoltaic qualities is the bombardment of $O_2$ species by PZ blends[3].

On the other hand, IPCE measurements serve as essential for assessing the performance of photovoltaic cells and understanding their efficiency under various illumination conditions[79]. Figure 10b depicts the IPCE characteristic curves of the resultant pristine (PZ0) and treated (PZ2 and PZ8) CEs -based DSSCs recorded at room temperature in the 300–800 nm region. At 573 nm, the produced PZ0, PZ2, and PZ8 CEs-based DSSCs'

IPCE values displayed the greatest value. Whereas the pristine PZ0 CE detected an IPCE value of around 15.6%. After plasma modification, the IPCE value rose to approximately 31.2% and 46.7%, respectively, as identified by DSSC using PZ2 and PZ8 CEs. Both the surface modification of PZ CEs with energetic oxygen plasma ions and the down-conversion function of the compact layer are responsible for this rise in IPCE value[80–82]. Additionally, it can be observed that the constructed DSSCs' current density values in Fig. 11a are in agreement with the highest IPCE values in Fig. 10b.

## Assessment of plasma-modified DSSCs performance

Exposing PZ Blends to various levels of $O_2$ plasma species enhanced cell efficiency via a variety of routes. Optimizing solar cell performance frequently requires maximizing charge transfer, light absorption, and overall device stability. To get the desired performance out of solar cells, these conditions must be targeted carefully. The apparatus for the I–V tester was utilized in conditions of a simulated solar spectrum executing 1000 W/m$^2$, with typical settings including an air mass (AM) of 1.5 G as well as a 25 °C temperature at ambient level. Hereafter, current flows in the solar cell circuit were monitored as a consequence of applied voltage, and white-light irradiance was stimulated. Table 3 delivers the associated PV variables, such as power conversion efficiency (η), fill factor (FF), open-circuit photovoltaic ($V_{oc}$), and short-circuit photocurrent density ($J_{sc}$), and Fig. 11 depicts the resultant photocurrent distribution–photovoltage (J–V) profiling curves[4]. Specifically, a gradual increase in $V_{oc}$ was observed with increasing plasma treatment duration on PZ CEs in DSSCs, that was caused by a combination of surface cleaning and defect passivation. The $O_2$-plasma passivates defects and dangling bonds on the ZnO surface. In more detail, these contaminants and defects function as recombination sites for charge carriers, lowering the solar cell's overall efficiency[60]. By cleaning and passivating the surface, the density of these defects and recombination were reduced, resulting in an increase in $V_{oc}$. Simultaneously, surface chemistry is modified by generating a thin oxide layer on the ZnO surface, which could enhance the material's electrical characteristics. This oxide layer increase energy alignment at the contact, resulting in greater charge transfer and separation, and therefore boosting the obtained voltage[56]. In addition to increasing carrier mobility, electrical conductivity, electron lifetime, and favourable work function changes[83]. These modifications result in more efficient charge transfer, lower series resistance, and lower recombination losses, all of which improve total solar cell efficiency. In this vein, the first DSSCs constructed with pristine CE (PZ0) attended the lowest power conversion efficiency (PCE) of 3.55% along with the smallest $J_{sc}$ of 10 mA/cm$^2$. Once the PZ CE received exposure to $O_2$ plasma dose for 2 min, the efficiency and $J_{sc}$ climbed to 4.63% and 12.7 mA/cm$^2$, respectively. In general, the electrical

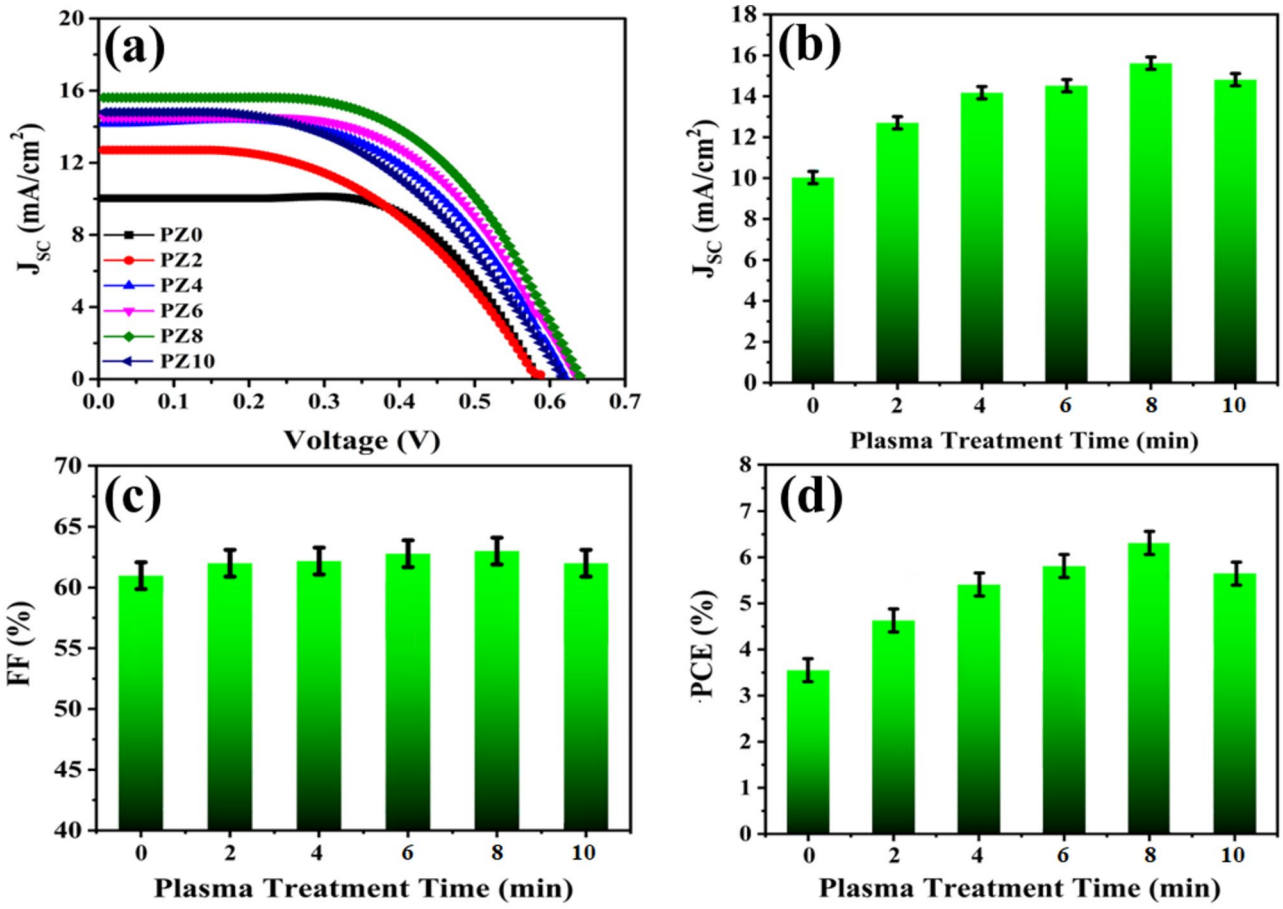


**Figure 11.** (**a**) J–V curves, (**b**) $J_{sc}$, (**c**) FF, and (**d**) PCE plots of DSSCs produced with PZ compounds subjected to different plasma doses.

properties and conductivity of a PAni compound changed after incorporating various functional groups (i.e., vacancies, O–H, and C-H groups) into its chemical structure[50]. While extrinsic doping (i.e., plasma species) involves treating a PAni composite after synthesis with dopants to change its electronic structure, intrinsic doping (i.e., ZnO nanofiller) involves adding dopant molecules or atoms during the polymer synthesis process to increase the number of charge carriers and create pathways for electron transport, thereby enhancing conductivity[56,61].

Mixing high energetic $O_2$ ions increased the mobility of charge carriers in PAni composites along with lowered charge carrier recombination through generating an environment that was conducive to charge dissociation[84]. Therefore, longer lifespans and more effective charge transfer inside the photovoltaic cell as a consequence of the increased mobility less resistive losses[60]. Additionally, in the complex PAni chain system, the well-distributed ZnO NPs inside the plasma atmosphere highlighted the energy levels[83]. By improving the flow of charge at contacts and capturing light in specific electromagnetic radiation areas, this alignment of energy levels boosts the efficiency of solar cells and the conversion of energy[59,60]. Along with their synergistic effects, the treated polymers' surfaces with high levels of ionic conductivity promoted ion activity, maintained the strength and resilience of the cell layers, shielded the active materials from degradation, alongside expanded the device's long-term efficacy. Expanded plasma treatment doses on CE surfaces improved PV cell performance even further: after 4 min at a plasma level, $\eta = 5.41\%$ was obtained, and after 6 min in a plasma environment, $\eta = 5.81\%$ was obtained. Whereas, excess plasma-ions may contribute to reducing charge carrier recombination, leading to longer lifetimes for generated charges and improved overall efficiency. In this respect, following 8 min of plasma surface modification of the PZ CE, the optimized efficiency of 6.31% and $J_{sc}$ of 15.6 mA/cm$^2$ were obtained. The improvement in efficiency equated to a proportion growth of 77% versus a pristine one. This gain was explained by the reality that suffusing a quantity of $O_2$ plasma free radicals into the PAni system developed continuous channels that enabled the mixture to move electrons more rapidly, hence raising the photovoltaic efficiency[84]. Enhancing π-π stacking interactions between PAni chains and lengthening the conjugation distance in the polymer backbone can both promote electron mobility[83]. Plus, a sharp rise in roughness of the surface values contributed to a reduction in reflected photons and, hence, a jump in generated charge carriers[12]. In agreement with morphological results, their poorer photo-generated electron transport characteristic may have contributed to the DSSC combined with pristine PZ CE's lowest photovoltaic efficiency, featuring an average grain size of 0.127 µm. Whenever the level of plasma ions within the PZ electrodes rose, the DSSCs displayed relatively good photovoltaic efficiency. This feature can be credited to the average grain size rise of the PZ hybrids, which may enable higher dye loading, more effective absorbency in the visible light area, as well as improved photo-generated electron transport due to conducting ions in the PZ composites[61]. On the other hand, prolonging plasma duration beyond 10 min dropped cell metrics, including $\eta = 6.33\%$ and $J_{sc} = 14.8$ mA/cm$^2$. Whereas, the photovoltaic efficiency was adversely affected by a further increase in the level of $O_2$ ions. The detrimental impact on the PV efficiency of PZ-10 min CE in DSSC can be explained by a significant increase in average particle size, which would undoubtedly reduce dye loading, visible light absorbance, as well as subsequent photogenerated electron generations[2]. Moreover, in order to ensure the reproducibility/repeatability of the created DSSCs, a minimum of six distinct devices were manufactured for plasma treated-PZ based CEs, which provided the best performance between composite-based CEs. The obtained data confirmed the reproducibility of both pristine and modified PZ-based DSSCs, as listed in Table 3.

Table 4 summarizes the photocurrent–voltage assessment of several types of PAni-based metal oxide composites used as CEs in DSSCs issued in the literature and compares their PV efficiency to that of the current DSSC created using a modified PZ material. When compared to the efficiency (6.31%) of the current PZ8 CEs-based DSSC, Table 4 shows that some of the DSSCs achieved lower performance. The presumed explanation for this enhancement in photovoltaic system efficiency might be ascribed to the considerably larger surface area of the plasma-treated PZ CEs, which could accommodate a high number of absorbing dye molecules[2].

## Conclusion

In this work, various $O_2$ plasma doses (0, 2, 4, 6, 8, and 10 min) were employed for developing innovative PZ-based CE in DSSCs, improving their microstructure and efficiency. Physical evaluations of the microstructure, porosity, morphology, contact angle, roughness, electrical, and optical, electrochemical impedance spectroscopy (EIS) features of CEs were conducted in along with an evaluation of J–V variables. The surface quality of the

| Entry | PAni-based CEs | $V_{oc}$ (V) | $J_{sc}$ (mA/cm$^2$) | FF (%) | H (%) | References |
|---|---|---|---|---|---|---|
| 1 | PAni-$MoSe_2$-rGO | 0.89 | 17.06 | 35 | 5.29 | [16] |
| 2 | PAni-$NiCo_2O_4$-rGO | 0.71 | 13.9 | 48 | 4.67 | [17] |
| 3 | PAni-rGO | 0.79 | 10.77 | 59 | 5.02 | [85] |
| 4 | PAni-rGO | 0.64 | 7.85 | 47 | 2.64 | [86] |
| 5 | PAni-Graphene @ Ni | 0.74 | 13.43 | 58 | 5.80 | [87] |
| 6 | PAni-$NiCo_2O_4$- rGO | 0.73 | 8.56 | 63 | 4.00 | [88] |
| 7 | PAni/rGO 40 wt.% | 0.63 | 12.58 | 55 | 3.98 | [89] |
| 8 | rGO/$SnO_2$ /PAni | 0.66 | 15.5 | 58 | 6.02 | [90] |
| 9 | PAni-ZnO (plasma for 8 min) | 0.64 | 15.62 | 63 | 6.31 | Present work |

**Table 4.** A comparison between the photocurrent–voltage assessment of PAni composite CEs used in DSSCs and their current study.

modified composites was progressively improved as the $O_2$ plasma level increased when compared to the pristine CE product, reaching a desirable level after 8 min (i.e., 0.2 µm for average pore size and average roughness Ra = 7.21 µm). In this regard, the PZ CE's maximum efficiency of 6.31% and $J_{sc}$ of 15.6 mA/cm$^2$ were attained after 8 min of plasma surface modification. Compared to a pristine one, the efficiency gain was equivalent to a 77% increase. This benefit was made clear by the fact that injecting a significant amount of plasma free radicals into the PAni system created continuous channels, thereby accelerated the mixture's electron-moving speed. Besides, an abundance of plasma ions might potentially limit charge carrier recombination, resulting in an extended lifespan for the produced charges and ultimately increasing cell efficiency achieving the desired solar cell performance.

## Data availability

Data is provided within the manuscript or supplementary information files.

Received: 27 May 2024; Accepted: 8 July 2024
Published online: 29 October 2024

## References

1. Alkuam, E., Mohammed, M. & Chen, T. Fabrication of CdS nanorods and nanoparticles with PANI for (DSSCs) dye-sensitized solar cells. *Sol. Energy* **150**, 317–324. https://doi.org/10.1016/j.solener.2017.04.056 (2017).
2. Kanimozhi, S., Prabu, K. M., Thambidurai, S. & Suresh, S. Dye-sensitized solar cell performance and photocatalytic activity enhancement using binary zinc oxide-copper oxide nanocomposites prepared via co-precipitation route. *Ceram. Int.* **47**(21), 30234–30246. https://doi.org/10.1016/j.ceramint.2021.07.203 (2021).
3. Zhu, S., Wei, W., Chen, X., Jiang, M. & Zhou, Z. Hybrid structure of polyaniline/ZnO nanograss and its application in dye-sensitized solar cell with performance improvement. *J. Solid State Chem.* **190**, 174–179. https://doi.org/10.1016/j.jssc.2012.02.028 (2012).
4. Ahmad, K. & Kim, H. A brief overview of electrode materials for hydrazine sensors and dye-sensitized solar cells. *Microchem. J.* **186**, 108317. https://doi.org/10.1016/j.microc.2022.108317 (2023).
5. Gülena, M. Rapid synthesis of SrTiO3 nanocubes and replacement of the high-cost platinum electrode with SrTiO3 @ PANI nanocomposite in dye-sensitized solar cells. *Synth. Met.* **293**, 117297. https://doi.org/10.1016/j.synthmet.2023.117297 (2023).
6. Areerob, Y. *et al.* Synthesis of novel MoWO4 with ZnO nanoflowers on multi-walled carbon nanotubes for counter electrode application in dye-sensitized solar cells. *Sci. Rep.* **12**(1), 1–11. https://doi.org/10.1038/s41598-022-16791-2 (2022).
7. Saadat, F., Alizadeh, A., Roudgar-Amoli, M. & Shariatinia, Z. Exploring the influence of Zn2SnO4/ZIF-8 nanocomposite photoelectrodes on boosting efficiency of dye sensitized solar cells. *Ceram. Int.* **48**(15), 21853–21864. https://doi.org/10.1016/j.ceramint.2022.04.165 (2022).
8. Khir, H. *et al.* Improved charge transfer through the minimal addition of Pb as a sintering aid to TiO2-based low-temperature dye sensitised solar cell. *Ceram. Int.* **49**(11), 17620–17628. https://doi.org/10.1016/j.ceramint.2023.02.128 (2023).
9. Rashwan, G. M., Ebnalwaled, A. A., Saad, E. M. & Shahat, M. A. Ca/Sn concentration-dependent enhancement of barium titanate ferroelectric performance: A dielectric and microstructural study. *J. Sol-Gel Sci. Technol.* **1**, 1–13 (2024).
10. Wang, C. C., Zhu, Y., Hu, Y. M., Dong, M. R. & Liu, J. K. Selenization treatment on Ag8SnSxSe6-x counter electrode of dye-sensitized solar cells in improving its electron transfer and electrocatalytic activity. *Ceram. Int.* **49**(13), 21804–21814. https://doi.org/10.1016/j.ceramint.2023.04.002 (2023).
11. Khalili, S., Afkhami, A. & Madrakian, T. Electrochemical simultaneous treatment approach: Electro-reduction of CO2 at Pt/PANI@ZnO paired with wastewater electro-oxidation over PbO2. *Appl. Catal. B Environ.* **328**, 122545 (2023).
12. El-Hossary, F. M., Ghitas, A., Abd El-Rahman, A. M., Ebnalwaled, A. A. & Shahat, M. A. Characterization and performance of PAni-TiO2 photovoltaic cells treated by RF plasma. *IOP Conf. Ser. Mater. Sci. Eng.* **1**, 12003 (2020).
13. Lin, T., Lv, X., Hu, Z., Xu, A. & Feng, C. Semiconductor metal oxides as chemoresistive sensors for detecting volatile organic compounds. *Sensors* **19**(2), 233 (2019).
14. Korotcenkov, G. Metal oxides for solid-state gas sensors: What determines our choice? *Mater. Sci. Eng. B* **139**(1), 1–23 (2007).
15. Ananikov, V. P. Organic–inorganic hybrid nanomaterials. *Nanomaterials* **9**(9), 1197 (2019).
16. Singh, A., Poddar, D., Thakur, S. & Jha, R. Ternary composite based on MoSe 2-rGO/polyaniline as an efficient counter electrode catalyst for dye sensitized solar cells. *Mater. Chem. Phys.* **273**, 125043. https://doi.org/10.1016/j.matchemphys.2021.125043 (2021).
17. Manikandan, V. S., Kumar, S., Palai, A. K., Mohanty, S. & Nayak, S. K. Ternary composite based on NiCo2 O4/rGO/PANI as an e ffi cient Pt free tri-iodide reducing agent for dye-sensitized solar cell application. *J. Photochem. Photobiol. A Chem.* **382**, 111939. https://doi.org/10.1016/j.jphotochem.2019.111939 (2019).
18. Montallana, A. D. S., Lai, B.-Z., Chu, J. P. & Vasquez, M. R. Jr. Enhancement of photodegradation efficiency of PVA/TiO2 nanofiber composites via plasma treatment. *Mater. Today Commun.* **24**, 101183 (2020).
19. Osonio, A. P. & Vasquez, M. R. Jr. Plasma-assisted reduction of silver ions impregnated into a natural zeolite framework. *Appl. Surf. Sci.* **432**, 156–162 (2018).
20. El-Hossary, F. M., Ghitas, A., El-Rahman, A. M. A., Shahat, M. A. & Fawey, M. H. The effective reduction of graphene oxide films using RF oxygen plasma treatment. *Vacuum* **188**, 158. https://doi.org/10.1016/j.vacuum.2021.110158 (2021).
21. Khosravi, A., Ghorbani, M. & Soleimani, M. Facile synthesize of PANI/GO/CuFe2 O4 nanocomposite material with synergistic effect for superb performance supercapacitor. *Electrochim. Acta* **439**, 141685. https://doi.org/10.1016/j.electacta.2022.141685 (2023).
22. Yang, C. *et al.* Enhanced photocatalytic activity of PANI/TiO2 due to their photosensitization-synergetic effect. *Electrochim. Acta* **247**, 486–495 (2017).
23. Niknezhad, A., Nabian, N. & Soleimani, M. PANI-ZnO/Pt–Ru electrocatalyst for methanol oxidation: Synthesis, characterization, electrocatalytic performance and artificial neural network modeling. *Chem. Eng. Res. Des.* **180**, 123–133. https://doi.org/10.1016/j.cherd.2022.02.010 (2022).
24. Rahman, K. H. & Kar, A. K. Titanium-di-oxide (TiO2) concentration-dependent optical and morphological properties of PAni-TiO2 nanocomposite. *Mater. Sci. Semicond. Process.* **105**, 104745 (2020).
25. El-Hossary, F. M. *et al.* Enhancement of adhesion force and surface conductivity of graphene oxide films using different solvents. *IOP Conf. Mater. Sci. Eng.* **762**, 012001. https://doi.org/10.1088/1757-899X/762/1/012001 (2020).
26. Shahat, M. A., Ahmed, Y. M. Z., Ghitas, A., El-Shater, A. & Soliman, W. Improving the thermophysical aspects of innovative clay brick composites for sustainable development via TiO2 and rGO nanosheets. *Constr. Build. Mater.* **401**, 132981 (2023).
27. El-Hossary, F. M. *et al.* Effect of UV-activated TiO2 nanoparticles on the properties and performance of PAni-TiO2 nanocomposite films for solar cell applications. *IOP Conference Series: Mater. Sci. Eng.* **956**, 12015 (2020).
28. Bednarczyk, K. *et al.* Effect of polyaniline content and protonating dopants on electroconductive composites. *Sci. Rep.* **11**(1), 7487 (2021).
29. Maity, J., Roy, D. & Bala, T. Template-free synthesis of hexagonal ZnO disk and ZnO–Ag composite as potential photocatalyst. *Hybrid Adv.* **1**, 100055 (2023).

30. Mahato, N., Parveen, N. & Cho, M. H. Synthesis of highly crystalline polyaniline nanoparticles by simple chemical route. *Mater. Lett.* **161**, 372–374 (2015).
31. Kandulna, R. & Choudhary, R. B. Concentration-dependent behaviors of ZnO-reinforced PVA–ZnO nanocomposites as electron transport materials for OLED application. *Polym. Bull.* **75**(7), 3089–3107. https://doi.org/10.1007/s00289-017-2186-9 (2018).
32. Basavaraja, C., Pierson, R., Huh, D. S., Venkataraman, A. & Basavaraja, S. Studies on properties of polyaniline-dodecylbenzene sulfonic acid composite films synthesized using different oxidants. *Macromol. Res.* **17**(8), 609–615 (2009).
33. Buerger, M. J. & and Azaroff, L. V. *The Powder Method in X-ray Crystallography* (1958).
34. Thomas, D., Fernandez, N. B., Mullassery, M. D. & Surya, R. Biochar-ZnO/polyaniline composite in energy storage application: Synthesis, characterization and electrochemical analysis. *Results Chem.* **6**, 101061 (2023).
35. Al-Masoud, M. A., Khalaf, M. M., Mohamed, I. M. A., Shalabi, K. & Abd El-Lateef, H. M. Computational, kinetic, and electrochemical studies of polyaniline functionalized ZnO and ZnO-SiO2 nanoparticles as corrosion protection films on carbon steel in acidic sodium chloride solutions. *J. Ind. Eng. Chem.* **112**, 398–422 (2022).
36. Aghris, S. *et al.* An electrochemical sensor based on clay/graphene oxide decorated on chitosan gel for the determination of flubendiamide insecticide. *Mater. Chem. Phys.* **296**, 127243. https://doi.org/10.1016/j.matchemphys.2022.127243 (2023).
37. Arora, R., Mandal, U. K., Sharma, P. & Srivastav, A. Effect of fabrication technique on microstructure and electrical conductivity of polyaniline-TiO2-PVA composite material. *Procedia Mater. Sci.* **6**, 238–243 (2014).
38. Olad, A., Behboudi, S. & Entezami, A. A. Preparation, characterization and photocatalytic activity of TiO2/polyaniline core-shell nanocomposite. *Bull. Mater. Sci.* **35**(5), 801–809 (2012).
39. Al-Ghamdi, A. A., Mahmoud, W. E., Yaghmour, S. J. & Al-Marzouki, F. M. Structure and optical properties of nanocrystalline NiO thin film synthesized by sol–gel spin-coating method. *J. Alloys Compd.* **486**(1–2), 9–13 (2009).
40. Akimov, Y. A. & Koh, W. S. Resonant and nonresonant plasmonic nanoparticle enhancement for thin-film silicon solar cells. *Nanotechnology* **21**(23), 235201 (2010).
41. Querol, X. *et al.* Environmental characterization of burnt coal gangue banks at Yangquan, Shanxi Province, China. *Int. J. Coal Geol.* **75**(2), 93–104 (2008).
42. Wu, Y. *et al.* Syntheses of four novel silicate-based nanomaterials from coal gangue for the capture of CO2. *Fuel* **258**, 116192. https://doi.org/10.1016/j.fuel.2019.116192 (2019).
43. Soliman, W. & Shahat, M. A. Optimizing the thermophysical qualities of innovative clay–rGO composite bricks for sustainable applications. *Sci. Rep.* **13**(1), 1–12. https://doi.org/10.1038/s41598-023-48966-w (2023).
44. Tao, Y., Huang, C., Lai, C., Huang, C. & Yong, Q. Biomimetic galactomannan/bentonite/graphene oxide film with superior mechanical and fire retardant properties by borate cross-linking. *Carbohydr. Polym.* **245**, 116508. https://doi.org/10.1016/j.carbpol.2020.116508 (2020).
45. Anwar, A., Liu, X. & Zhang, L. Nano-cementitious composites modified with graphene oxide—A review. *Thin-Walled Struct.* **183**, 110326. https://doi.org/10.1016/j.tws.2022.110326 (2023).
46. Abdelhamied, M. M., Atta, A., Abdelreheem, A. M., Farag, A. T. M. & El Okr, M. M. Synthesis and optical properties of PVA/PANI/Ag nanocomposite films. *J. Mater. Sci. Mater. Electron.* **31**, 22629–22641 (2020).
47. Chitra, Laishram, R., Rajput, S. & Singh, K. C. Particle-size-induced high piezoelectricity in (Ba0.88Ca0.12)(Ti0.94Sn0.06)O3 piezoceramics prepared from nanopowders. *J. Alloys Compd.* **812**, 152128. https://doi.org/10.1016/j.jallcom.2019.152128 (2020).
48. Shahat, M. A., Ibrahim, M. A., Ghitas, A. & Ezzat, H. A. Designing innovative PAni-based adsorbents for CO2 capture via in-situ nitrogen plasma modification for sustainable development. *J. CO2 Util.* **84**, 102830 (2024).
49. Zhang, B. *et al.* Double-shell PANS@ PANI@ Ag hollow microspheres and graphene dispersed in epoxy with enhanced microwave absorption. *J. Mater. Sci. Mater. Electron.* **30**, 9785–9797 (2019).
50. Robertson, J. Diamond-like amorphous carbon. *Mater. Sci. Eng. R Rep.* **37**(4–6), 129–281 (2002).
51. Good, R. J. Contact angle, wetting, and adhesion: A critical review. *J. Adhes. Sci. Technol.* **6**(12), 1269–1302 (1992).
52. Reda, S. M. & Al-Ghannam, S. M. Synthesis and electrical properties of polyaniline composite with silver nanoparticles. *Adv. Mater. Phys. Chem.* **02**(02), 75–81. https://doi.org/10.4236/ampc.2012.22013 (2012).
53. Kulkarni, M. *et al.* Wettability studies of topologically distinct titanium surfaces. *Colloids Surf. B Biointerfaces* **129**, 47–53 (2015).
54. Carré, A. Polar interactions at liquid/polymer interfaces. *J. Adhes. Sci. Technol.* **21**(10), 961–981. https://doi.org/10.1163/156856107781393875 (2007).
55. Siddiqa, A. J., Chaudhury, K. & Adhikari, B. Hydrophilic low density polyethylene (LDPE) films for cell adhesion and proliferation. *Res. Rev. J. Med. Chem* **1**, 43–54 (2015).
56. Pereira, V. R. *et al.* Preparation of polysulfone-based PANI–TiO 2 nanocomposite hollow fiber membranes for industrial dye rejection applications. *RSC Adv.* **6**(102), 99764–99773 (2016).
57. El-Hossary, F. M. *et al.* Cold RF oxygen plasma treatment of graphene oxide films. *J. Mater. Sci. Mater. Electron.* https://doi.org/10.1007/s10854-021-06123-x (2021).
58. Jamshidinia, M. & Kovacevic, R. The influence of heat accumulation on the surface roughness in powder-bed additive manufacturing. *Surf. Topogr. Metrol. Prop.* **3**(1), 14003 (2015).
59. Ogurtsov, N. A. *et al.* Deep impact of the template on molecular weight, structure, and oxidation state of the formed polyaniline. *J. Phys. Chem. B* **117**(17), 5306–5314 (2013).
60. Pud, A. A. *et al.* On the importance of interface interactions in core-shell nanocomposites of intrinsically conducting polymers. *Semicond. Phys. Quantum Electron. Optoelectron.* **22**(4), 470 (2019).
61. Zagorny, M. & Bykov, I. Synthesis and electric properties of polyaniline-TiO2 nanocomposites. *J. Chem. Eng. Chem. Res.* **1**(1), 6–14 (2014).
62. Srikanth, K. S., Hooda, M. K., Singh, H., Singh, V. P. & Vaish, R. Structural and photocatalytic performance of (Ba, Ca) TiO3–Ba (Sn, Ti) O3 ferroelectric ceramics. *Mater. Sci. Semicond. Process.* **79**, 153–160 (2018).
63. Mir, F. A. Structural and optical properties of ZnS nanocrystals embedded in polyacrylamide. *J. Optoelectron. Biomed. Mater.* **2**(2), 79–84 (2010).
64. Xia, H. & Wang, Q. Ultrasonic irradiation: A novel approach to prepare conductive polyaniline/nanocrystalline titanium oxide composites. *Chem. Mater.* **14**(5), 2158–2165 (2002).
65. Su, S.-J. & Kuramoto, N. Processable polyaniline–titanium dioxide nanocomposites: Effect of titanium dioxide on the conductivity. *Synth. Met.* **114**(2), 147–153 (2000).
66. Cionti, C., Della Pina, C., Meroni, D., Falletta, E. & Ardizzone, S. Photocatalytic and oxidative synthetic pathways for highly efficient PANI-TIO2 nanocomposites as organic and inorganic pollutant sorbents. *Nanomaterials* **10**(3), 441. https://doi.org/10.3390/nano10030441 (2020).
67. Takpire, S. R. & Waghuley, S. A. Investigating the optical and structural properties of PANi/Ti polymer composites for photovoltaic application. *J. Energy Inst.* **90**(1), 44–50. https://doi.org/10.1016/j.joei.2015.11.001 (2017).
68. Pankove, J. I. *Optical Processes in Semiconductors* (Courier Corporation, 1975).
69. Cavalcante, L. S. *et al.* Microstructure, dielectric properties and optical band gap control on the photoluminescence behavior of Ba [Zr0.25 Ti0.75] O3 thin films. *J. Sol-Gel Sci. Technol.* **49**, 35–46 (2009).
70. Wang, Q. *et al.* Characteristics of high efficiency dye-sensitized solar cells. *J. Phys. Chem. B* **110**(50), 25210–25221 (2006).
71. Venkatesan, S., Manurung, D., Teng, H. & Lee, Y.-L. Efficiency and stability improvements for room light dye-sensitized solar cells in the presence of electrochemically fabricated composite counter electrodes. *J. Power Sources* **518**, 230781 (2022).

72. Zhang, H. & Zhu, Y. Significant visible photoactivity and antiphotocorrosion performance of CdS photocatalysts after monolayer polyaniline hybridization. *J. Phys. Chem. C* **114**(13), 5822–5826 (2010).
73. Chen, X., Zhang, Y., Cai, J. & Zhu, J. In situ grown hierarchical NiCo2O4@ MnMoO4 core–shell nanoarrays on carbon cloth as high-performance counter electrode for dye-sensitized solar cells. *Sol. Energy* **227**, 616–624 (2021).
74. Yildiz, A. *et al.* Efficient iron phosphide catalyst as a counter electrode in dye-sensitized solar cells. *ACS Appl. Energy Mater.* **4**(10), 10618–10626 (2021).
75. Gnanasekar, S. & Grace, A. N. Titanium nitride nanoflower buds as Pt-free counter electrodes for dye-sensitized solar cells. *ACS Appl. Nano Mater.* **4**(8), 8251–8261 (2021).
76. Peter, I. J., Vijaya, S., Anandan, S. & Nithiananthi, P. Sb2S3 entrenched MWCNT composite as a low-cost Pt-free counter electrode for dye-sensitized solar cell and a viewpoint for a photo-powered energy system. *Electrochim. Acta* **390**, 138864 (2021).
77. Wang, Y., Xu, J., Zong, W. & Zhu, Y. Enhancement of photoelectric catalytic activity of TiO2 film via polyaniline hybridization. *J. Solid State Chem.* **184**(6), 1433–1438 (2011).
78. Sutar, D. S., Lenfant, S., Vuillaume, D. & Yakhmi, J. V. Electronic structure of highly crystalline polyaniline by study of tunneling conduction in n+-Si/self-assembled monolayer/polyaniline heterostructures. *Org. Electron.* **9**(5), 602–608 (2008).
79. Akman, E. *et al.* Improving performance and stability in quantum dot-sensitized solar cell through single layer graphene/Cu2S nanocomposite counter electrode. *Renew. Energy* **145**, 2192–2200. https://doi.org/10.1016/j.renene.2019.07.150 (2020).
80. Akman, E. Enhanced photovoltaic performance and stability of dye-sensitized solar cells by utilizing manganese-doped ZnO photoanode with europium compact layer. *J. Mol. Liq.* **317**, 114223. https://doi.org/10.1016/j.molliq.2020.114223 (2020).
81. Ari, D. A. *et al.* Design of an amorphous ZnWSe 2 alloy-based counter electrode for highly efficient dye-sensitized solar cells. *Mater. Chem. Front.* **7**(18), 4120–4131 (2023).
82. Akman, E. & Karapinar, H. S. Electrochemically stable, cost-effective and facile produced selenium@activated carbon composite counter electrodes for dye-sensitized solar cells. *Sol. Energy* **234**, 368–376. https://doi.org/10.1016/j.solener.2022.02.011 (2022).
83. Su, B., Min, S., She, S., Tong, Y. & Bai, J. Synthesis and characterization of conductive polyaniline/TiO2 composite nanofibers. *Front. Chem. China* **2**(2), 123–126. https://doi.org/10.1007/s11458-007-0025-5 (2007).
84. Ferrag, C., Noroozifar, M., Modarresi-Alam, A. R. & Kerman, K. Graphene oxide hydrogel electrolyte for improving the performance of electropolymerized polyaniline solar cells. *J. Power Sources* **542**, 231796. https://doi.org/10.1016/j.jpowsour.2022.231796 (2022).
85. Mohan, K., Bora, A., Roy, R. S., Nath, B. C. & Dolui, S. K. Polyaniline nanotube/reduced graphene oxide aerogel as efficient counter electrode for quasi solid state dye sensitized solar cell. *Sol. Energy* **186**, 360–369 (2019).
86. Park, N.-G. Perovskite solar cells: An emerging photovoltaic technology. *Mater. Today* **18**(2), 65–72 (2015).
87. Chen, X., Liu, J., Qian, K. & Wang, J. Ternary composites of Ni–polyaniline–graphene as counter electrodes for dye-sensitized solar cells. *RSC Adv.* **8**(20), 10948–10953 (2018).
88. Kwon, W., Kim, J.-M. & Rhee, S.-W. Electrocatalytic carbonaceous materials for counter electrodes in dye-sensitized solar cells. *J. Mater. Chem. A* **1**(10), 3202–3215 (2013).
89. Seema, H., Zafar, Z. & Samreen, A. Evaluation of solution processable polymer reduced graphene oxide transparent films as counter electrodes for dye-sensitized solar cells. *Arab. J. Chem.* **13**(4), 4978–4986. https://doi.org/10.1016/j.arabjc.2020.01.020 (2020).
90. Dissanayake, M. A. K. L., Kumari, J. M. K. W., Senadeera, G. K. R. & Anwar, H. Low cost, platinum free counter electrode with reduced graphene oxide and polyaniline embedded SnO2 for efficient dye sensitized solar cells. *Sol. Energy* **230**, 151–165. https://doi.org/10.1016/j.solener.2021.10.022 (2021).


## Acknowledgements

The authors would like to thank the Deanship of Scientific Research at Shaqra University, Kingdom of Saudi Arabia, for supporting this work. They also thank the National Research Institute of Astronomy and Geophysics (NRIAG), Egypt, for their support.

## Author contributions

Fahad N. Almutairi: Writing—original draft, Formal analysis. Ahmed Ghitas: Methodology, Supervision. Nadi Mlihan Alresheedi: Writing—review & editing, Validation. M. Abdelhamid Shahat: Methodology, Writing—original draft, Writing—review & editing.

## Competing interests

The authors declare no competing interests.

## Additional information

**Correspondence** and requests for materials should be addressed to M.A.S.

**Reprints and permissions information** is available at www.nature.com/reprints.

**Publisher's note** Springer Nature remains neutral with regard to jurisdictional claims in published maps and institutional affiliations.